Article:

Morgado, E, Morgan, DJ orcid.org/0000-0002-7292-2536, Harvey, J orcid.org/0000-0002-0390-3438 et al. (6 more authors) (2022) The Magmatic Evolution and the Regional Context of the 1835 AD Osorno Volcano Products (41°06'S, Southern Chile). Journal of Petrology, 63 (11). egac105. ISSN 0022-3530

https://doi.org/10.1093/petrology/egac105

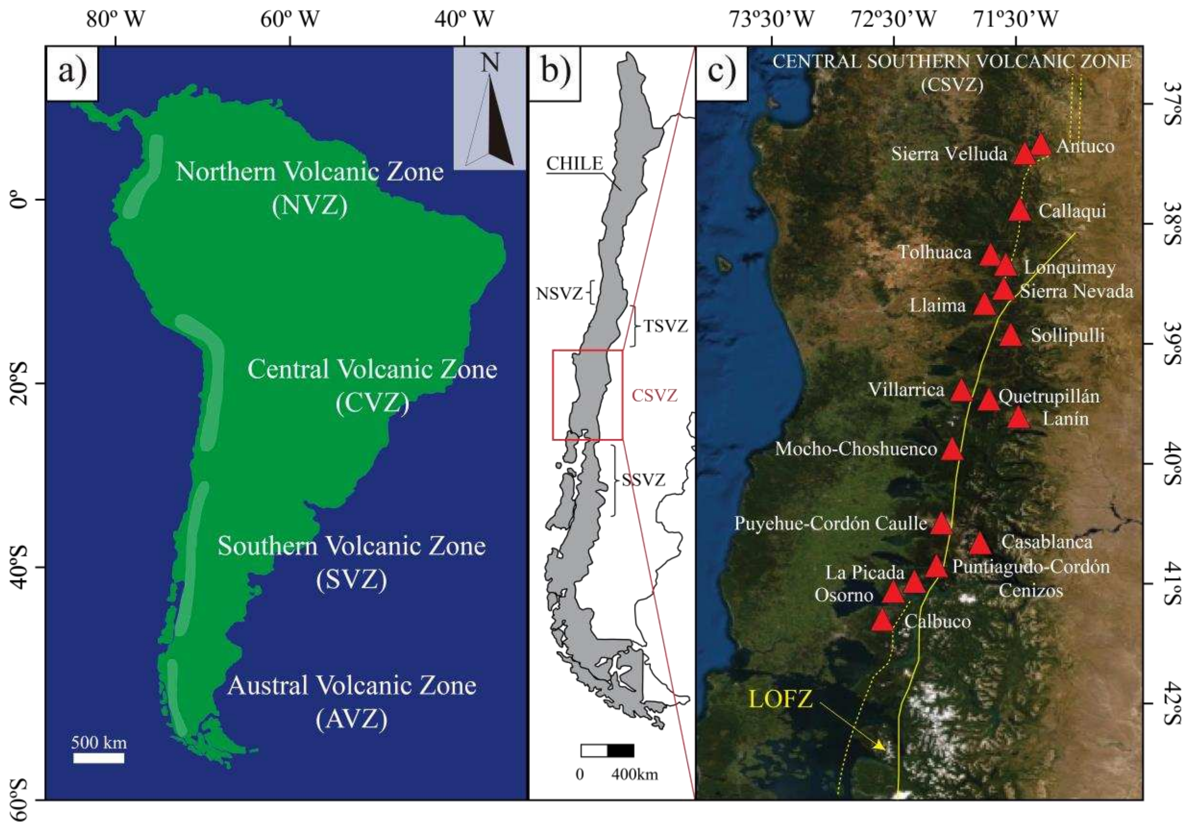

Figure 1. a) Location of the different volcanic zones of the Andes. b) Location of the four subdivisions of the Southern Volcanic Zone. c) The Central Southern Volcanic Zone and location of stratovolcanoes and the Liquiñe-Ofqui Fault Zone (LOFZ). Location of the LOFZ (solid and dashed lines) inferred from Cembrano et al. (1996) and Cembrano and Lara (2009).

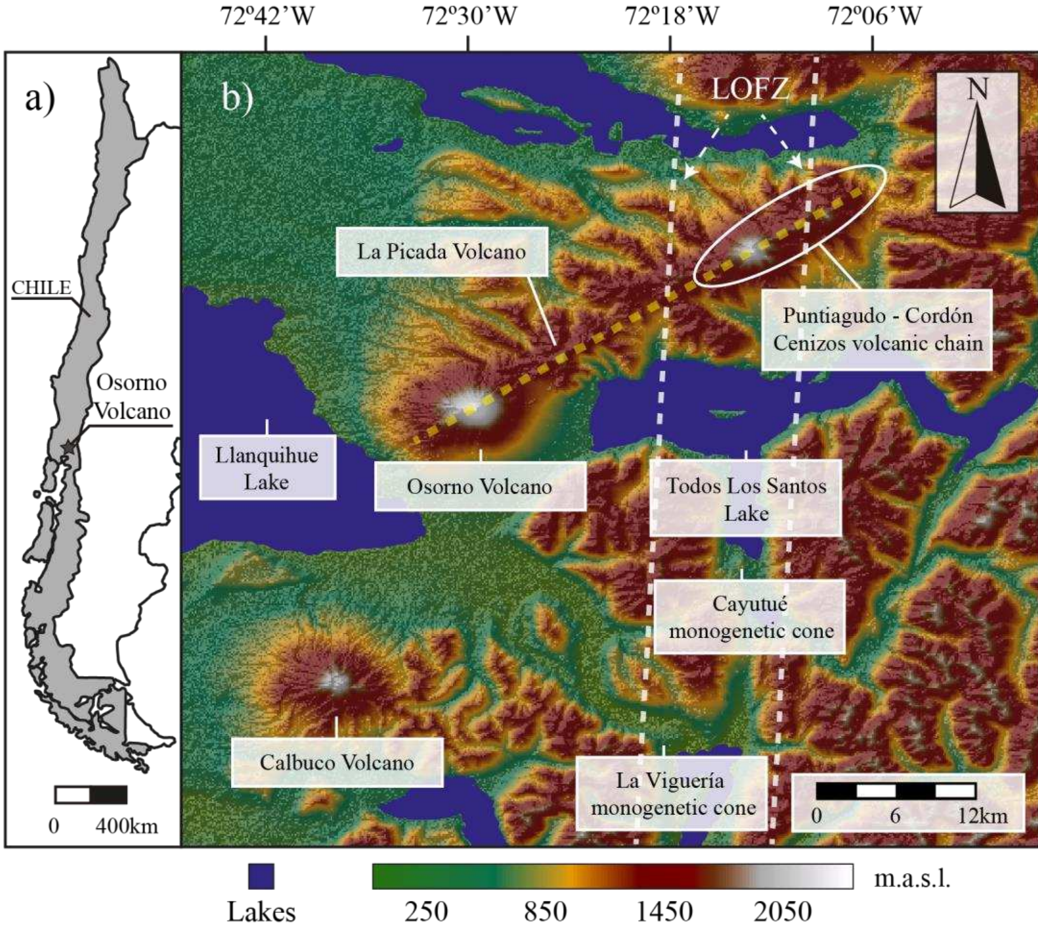

Figure 2. (a) Location of the Osorno volcano in Chile. (b) Location of Osorno, La Picada, Puntiagudo, and Calbuco volcanoes and Cordón Cenizos volcanic chain, La Viguería cone, and the Liquiñe-Ofqui Fault Zone (LOFZ, white dashed line). The alignment of Osorno, La Picada, Puntiagudo and Cordón Cenizos is represented by a yellow, dashed line. Advanced Spaceborne Thermal Emission and Reflection Radiometer (ASTER) Global Digital Elevation Model (GDEM) image was obtained via EarthExplorer, USGS (http://earthexplorer.usgs.gov).

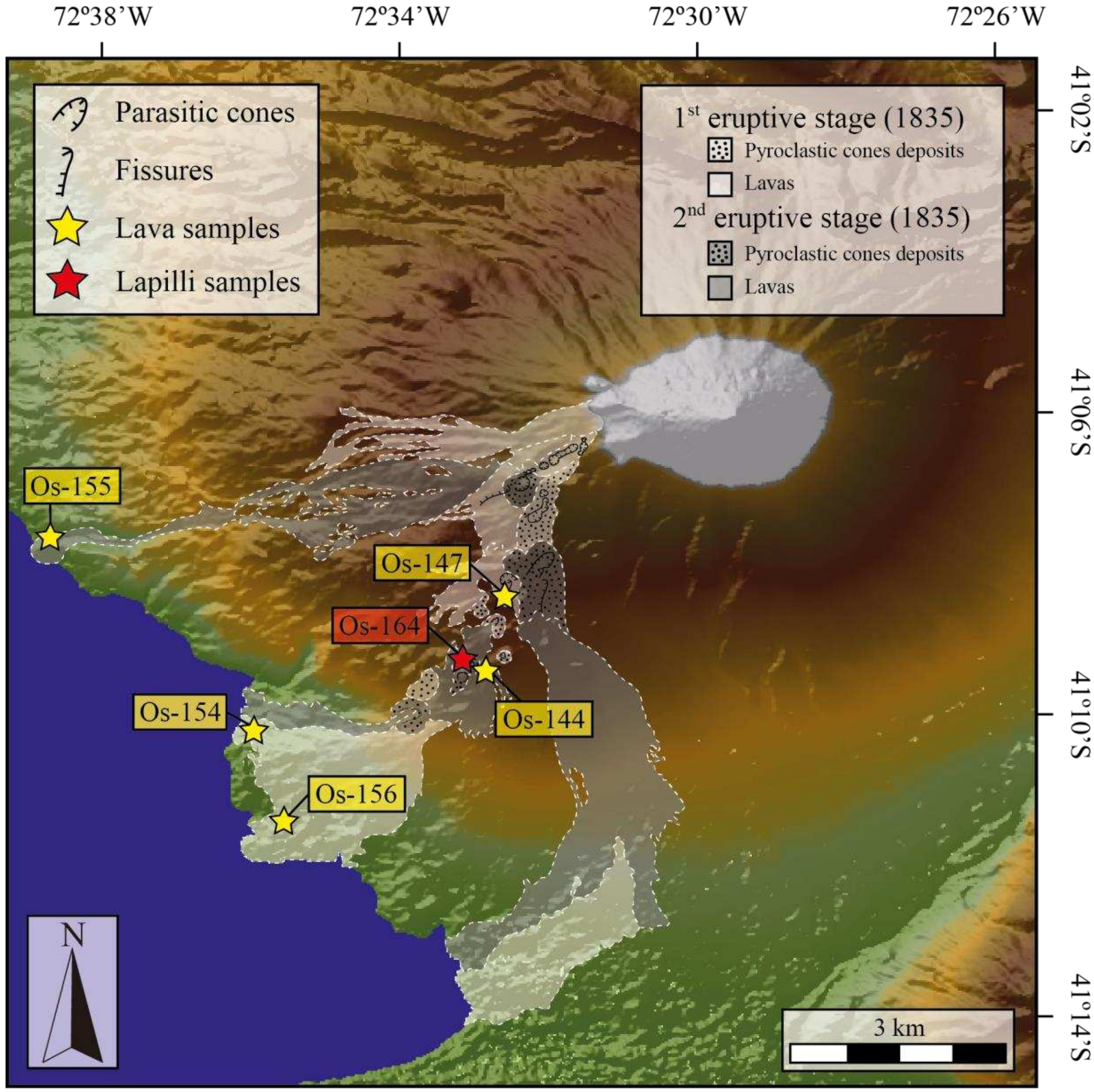

Figure 3. Osorno volcano and the deposits of the first and second stages of the 1835 eruption. Yellow stars represent locations where samples are collected from a lava flow, whereas lapilli sample locations are represented by red stars. Locations and dates of the lava flows and fall deposits are based on Moreno et al. (2010) and Lara et al. (2012). ASTER–GDEM image from EarthExplorer, USGS (http://earthexplorer.usgs.gov).

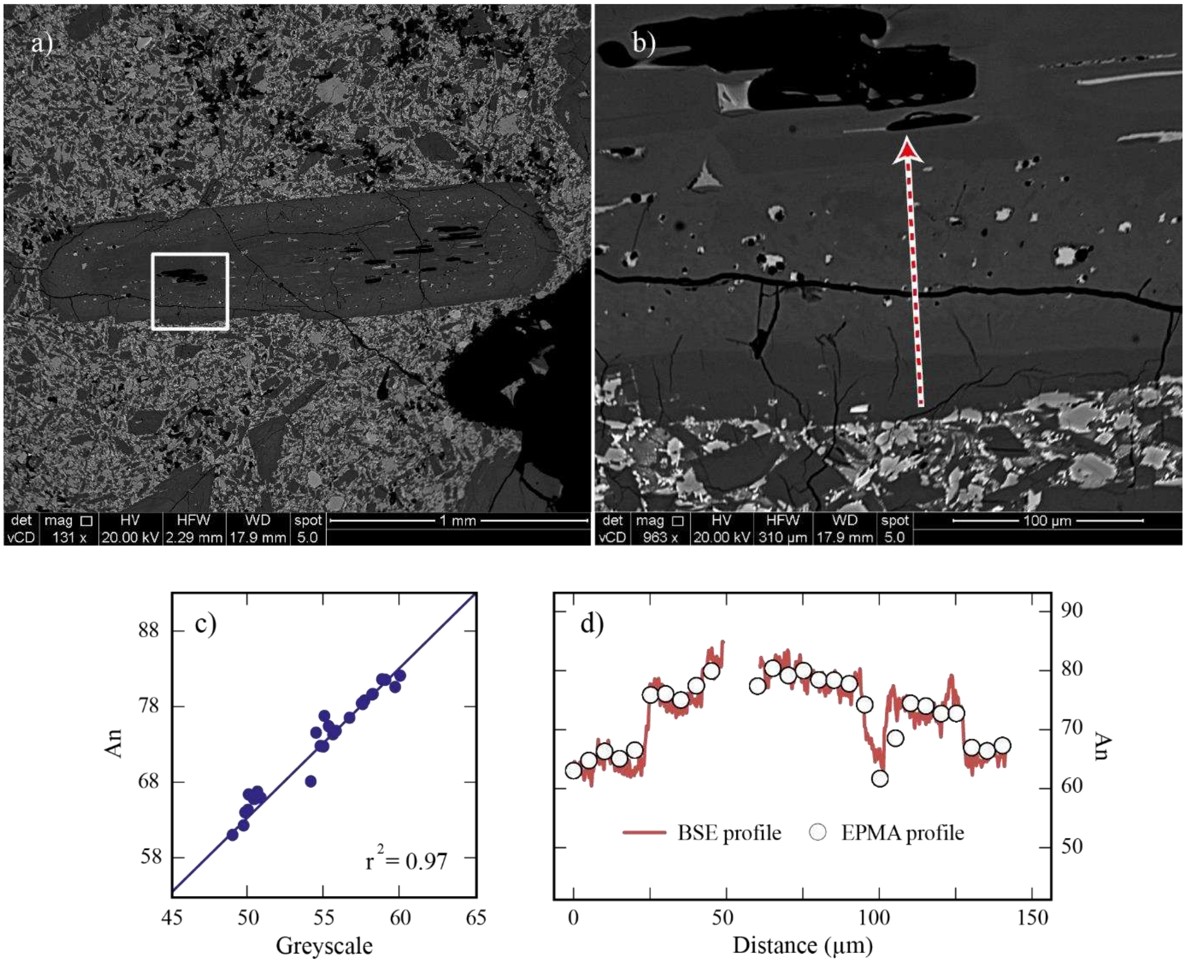

Figure 4. (a) Backscatter electron (BSE) images of an isolated plagioclase phenocryst where different compositional zones are found. Brighter greyscale colours are correlated to higher density. (b) The arrow represents the profile measured by electron probe micro-analysis (EPMA) and its direction. (c) Relation and coefficient of determination (r^2) between BSE greyscale profile and the measured anorthite content (An = 100×Ca/(Ca+Na+K); in molar proportions). "An" is a representative description of the composition of plagioclase because in all crystals the K content remains constant throughout (details in Supplementary Data 2). (d) Anorthite profile composition (An) by EPMA of the measured profile (circles) coupled with the BSE profile based on greyscale values calibrated with the composition measured by electron microprobe (solid line).

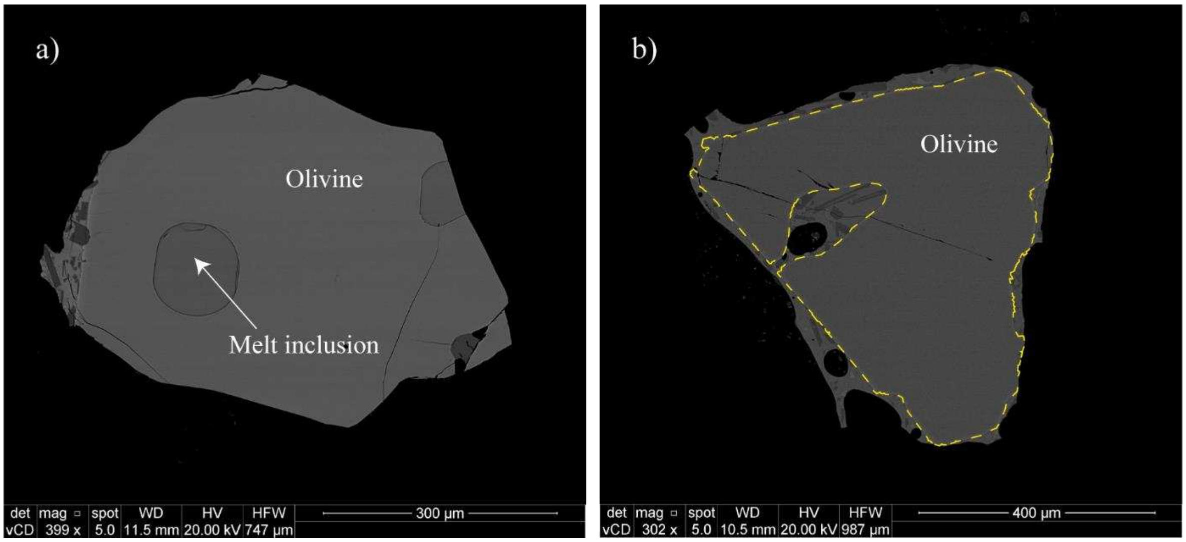

Figure 5. (a) Olivine-hosted melt inclusion of ~110 µm diameter. (b) Resorption feature (embayment) in olivine phenocryst with glass and plagioclase microlites. The yellow dashed line represents the olivine grain boundary.

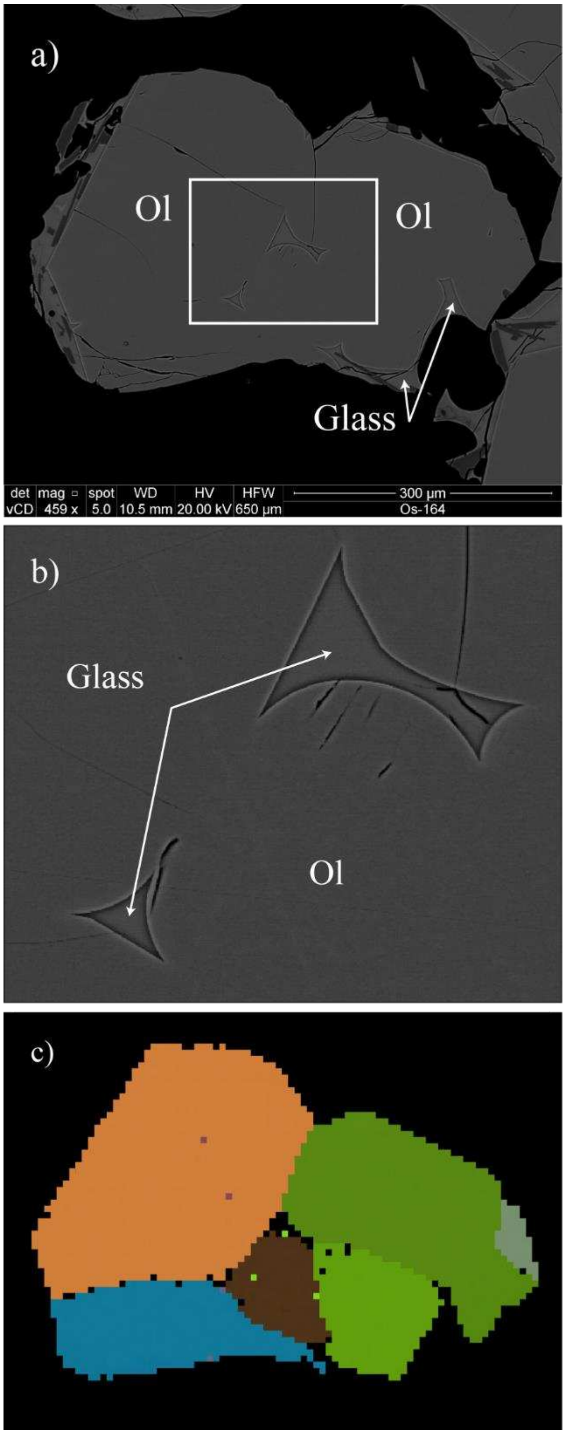

Figure 6. (a) BSE image of a crystal clot of olivine grains. (b) Zoom of the BSE image, which shows interstitial glass between the crystals constituting the clot. (c) EBSD map represents the diversity of olivine crystal orientations, consistent with the observation that the glasses are interstitial and are not melt inclusions.

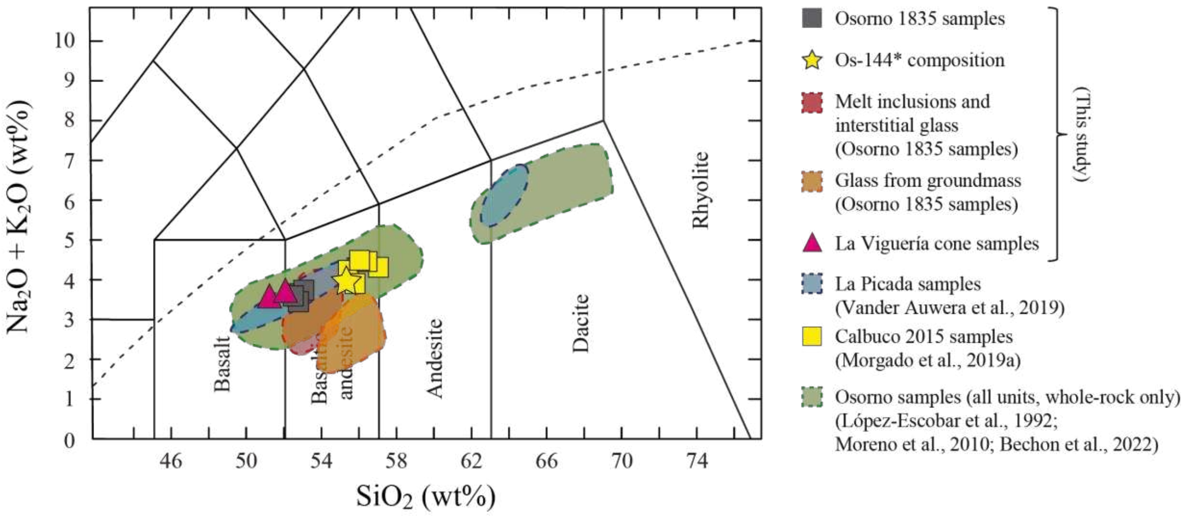

Figure 7. Total alkali versus silica (Le Bas et al., 1986) plots of the Osorno 1835 volcanic products (grey squares), the modified composition of Os-144 (Os-144*, yellow star), melt inclusions (Group 1 of glass, red field), and glass from groundmass (Group 2 glass, green field), La Viguería cone products (pink triangles), La Picada volcanic products (Vander Auwera et al., 2019, blue field), and Calbuco 2015 volcanic products (Morgado et al., 2019a, yellow squares).

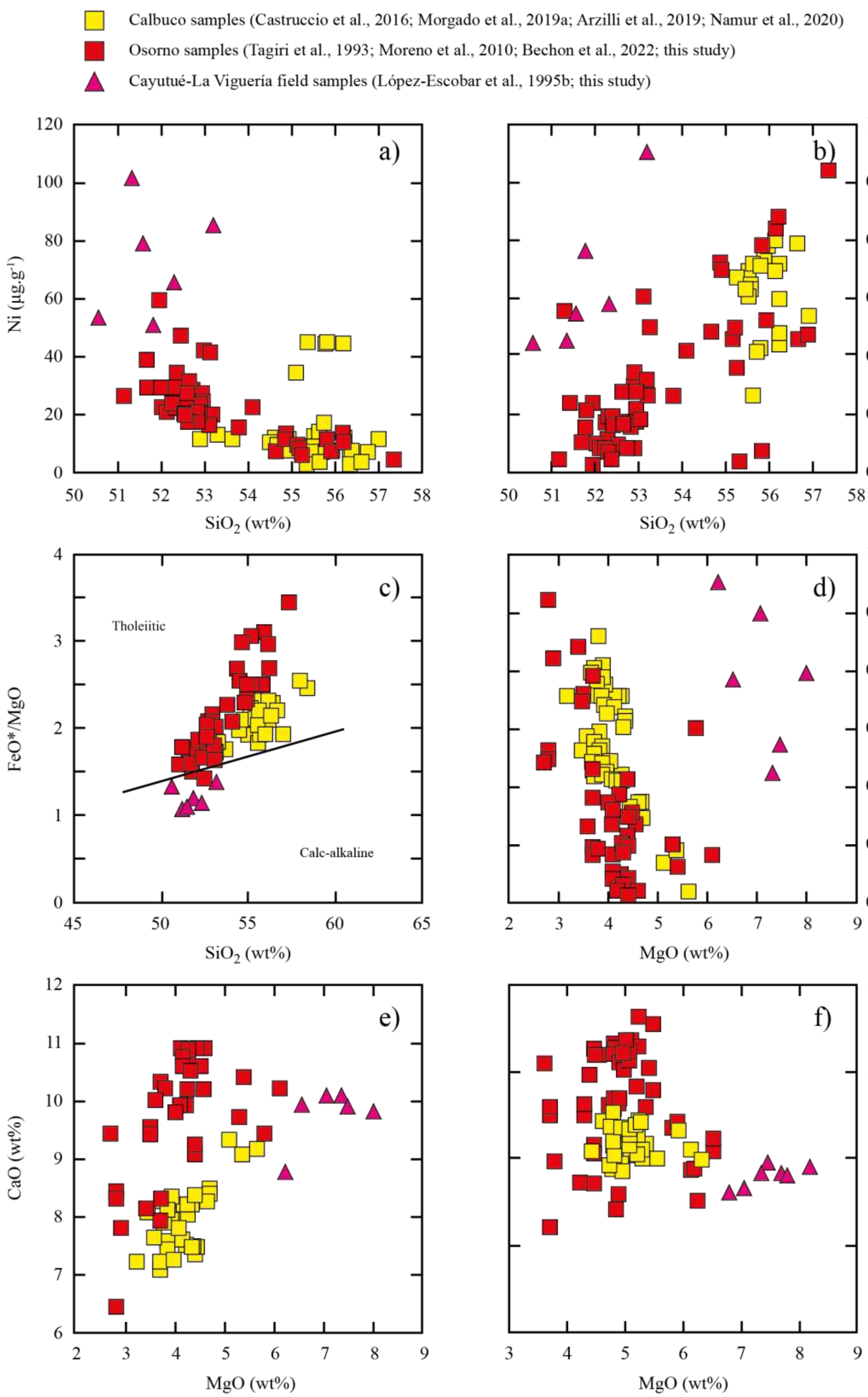

Calbuco samples (Castruccio et al., 2016; Morgado et al., 2019a; Arzilli et al., 2019; Namur et al., 2020)
Osorno samples (Tagiri et al., 1993; Moreno et al., 2010; Bechon et al., 2022; this study)
Cayutué-La Viguería field samples (López-Escobar et al., 1995b; this study)
a)
b)
c)
d)
e)
f)
Ni (µg.g-1)
K_2O (wt%)
SiO_2 (wt%)
FeO*/MgO
Tholeiitic
Calc-alkaline
MgO (wt%)
CaO (wt%)
Al_2O_3 (wt%)

Figure 8. (a) Variations of Ni ($\mu g \cdot g^{-1}$) versus SiO_2 (wt. %), (b) K_2O (wt. %) versus SiO_2 (wt. %), (c) FeO*/MgO versus SiO_2 (wt. %), (d) K_2O (wt. %) versus MgO (wt. %), (e) CaO (wt. %) versus MgO (wt. %), and (f) Al_2O_3 (wt. %) versus MgO (wt. %) of Holocene erupted products from Calbuco volcano (Castruccio et al., 2016; Morgado et al., 2019a; Arzilli et al., 2019; Namur et al., 2020), Osorno volcano (Tagiri et al., 1993; Moreno et al., 2010; Bechon et al., 2022; this study), and Cayutué-La Viguería field (López-Escobar et al., 1995a; this study).

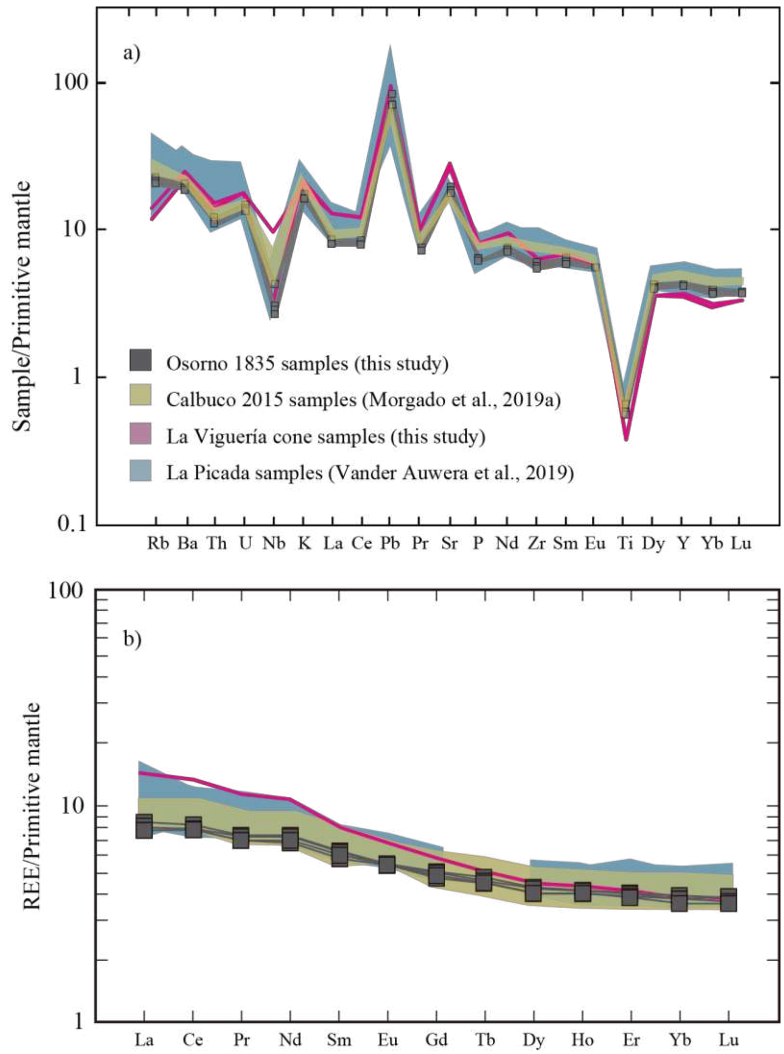

Figure 9. (a) Primitive mantle-normalised (Sun and McDonough, 1989) incompatible trace element diagram for Calbuco erupted products, taken from López-Escobar et al. (1995b) Morgado et al. (2019a). Major and trace element concentrations from Osorno and La Viguería are available in Table 2. (b) REE patterns of bulk rock samples from volcanic systems of the region (La Viguería, Osorno, Calbuco, and La Picada volcanoes).

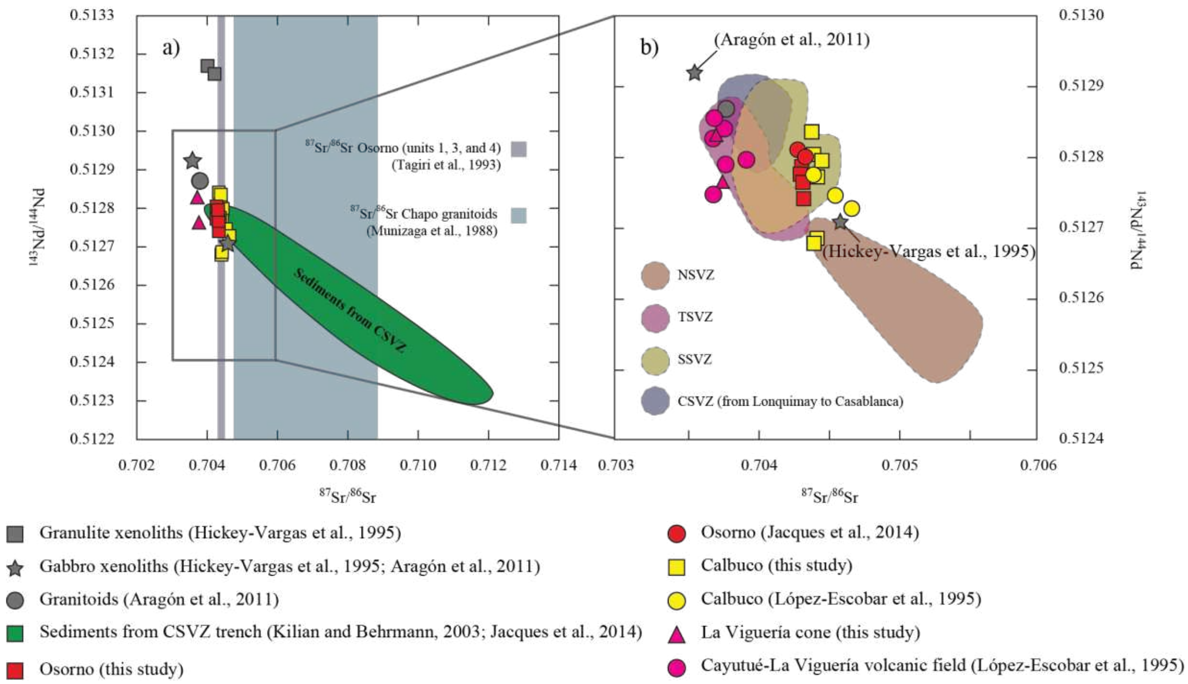

Figure 10. (a) ^{144}Nd/^{143}Nd versus ^{87}Sr/^{86}Sr of volcanic products of Osorno, Calbuco, sediments from the CSVZ trench, granulite xenoliths, gabbro xenoliths and from the basement, and granitoids from basement. (b) Comparison of ^{144}Nd/^{143}Nd versus ^{87}Sr/^{86}Sr with other volcanic zones from the SVZ (from Hickey-Vargas et al., 2016a and references therein).

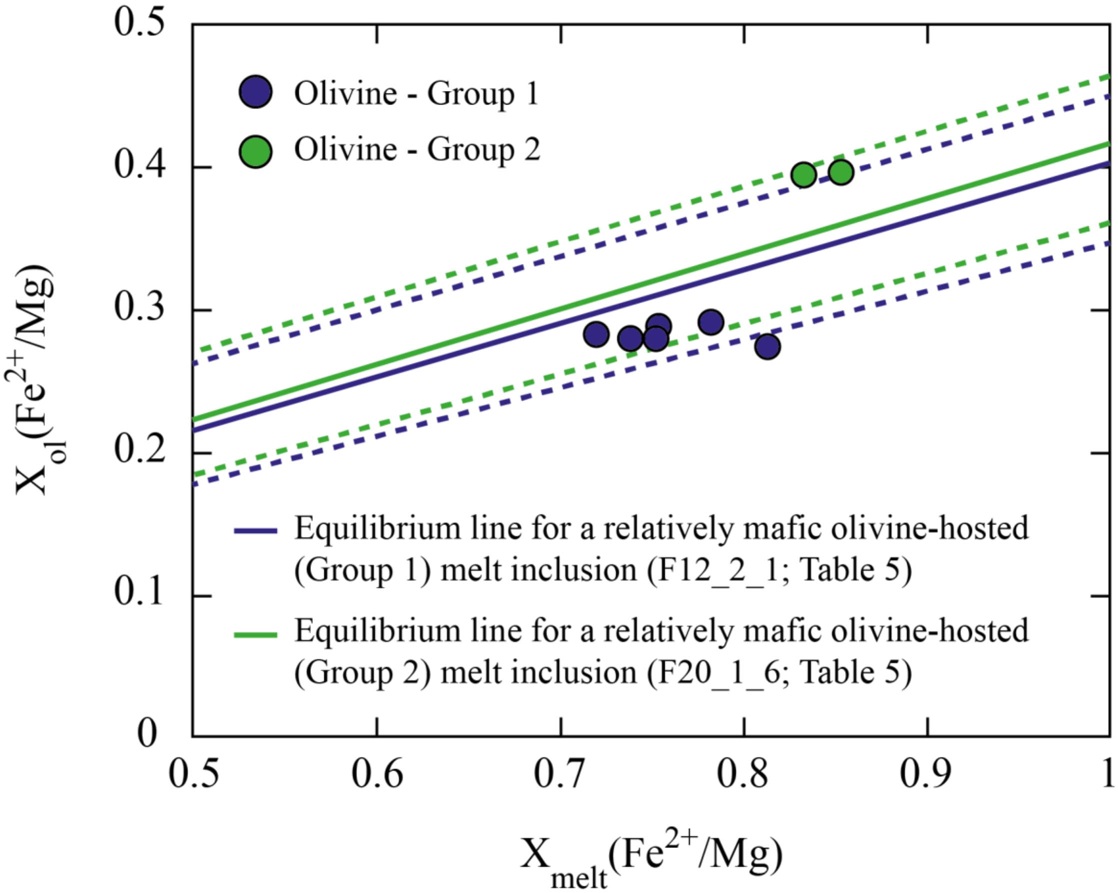

Figure 11. Olivine core compositions ($X_{ol}(Fe^{2+}/Mg)$ vs $X_{melt}(Fe^{2+}/Mg)$) for products of the 1835 Osorno eruption. Most of the olivine compositions from group 1 (Fo_{76-79}) are in equilibrium with the hosted melt inclusions, whereas the two olivine crystals from group 2 ($Fo_{69–73}$) are in equilibrium with the hosted melt inclusions. The Fe^{2+} in the melt is calculated using the olivine-hosted spinel inclusions Fe^{2+}/Fe^{3+}. We calculate the equilibrium lines as $X_{ol}(Fe^{2+}/Mg) = K_D \times X_{melt}(Fe^{2+}/Mg)$, where K_D is calculated via the Toplis (2005) procedure. Dashed lines represent the uncertainty of the Toplis (2005) method.

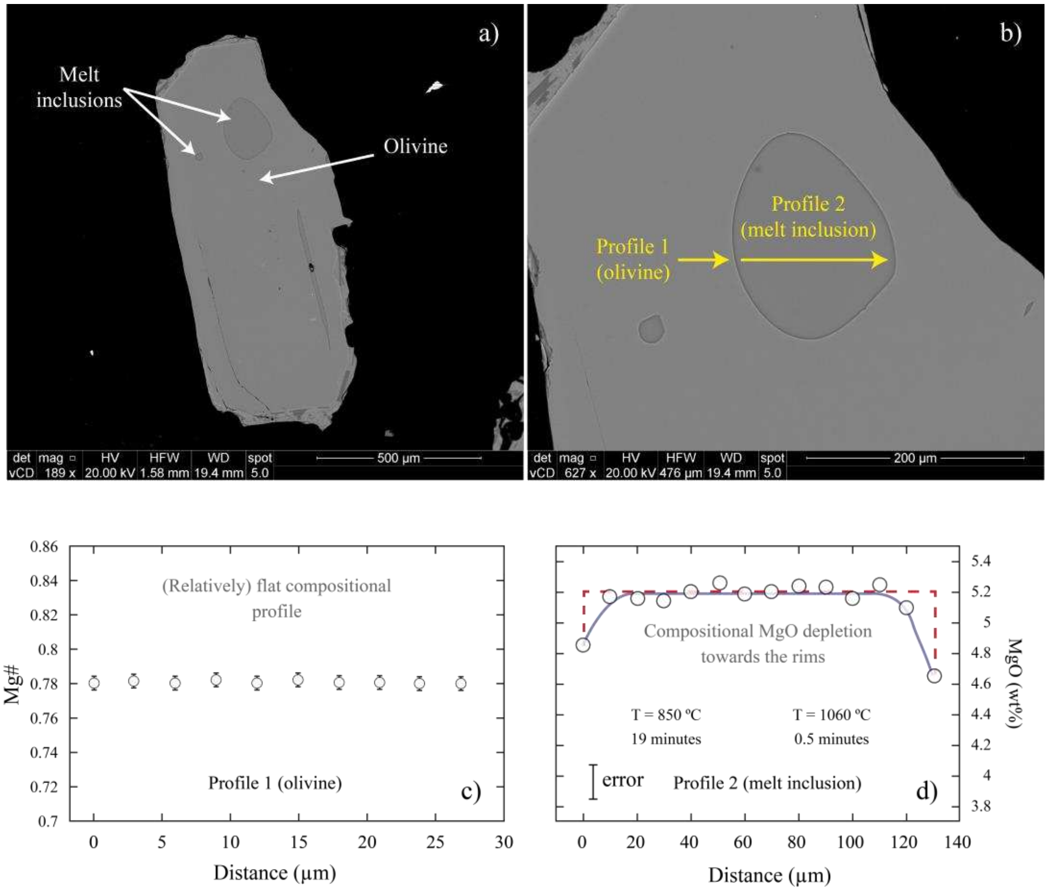

Figure 12. (a) BSE image of an olivine phenocryst and melt inclusions. (b) Zoom of the BSE image, which shows the EPMA profiles in olivine and large melt inclusion. (c) Mg# composition of olivine phenocryst traverse, which is flat (showing the absence of disequilibrium), (d) MgO (wt. %) composition profiles of the melt inclusion shown in b), which show depletion towards the rim. That depletion represents diffusion and the related timescales are a few minutes.

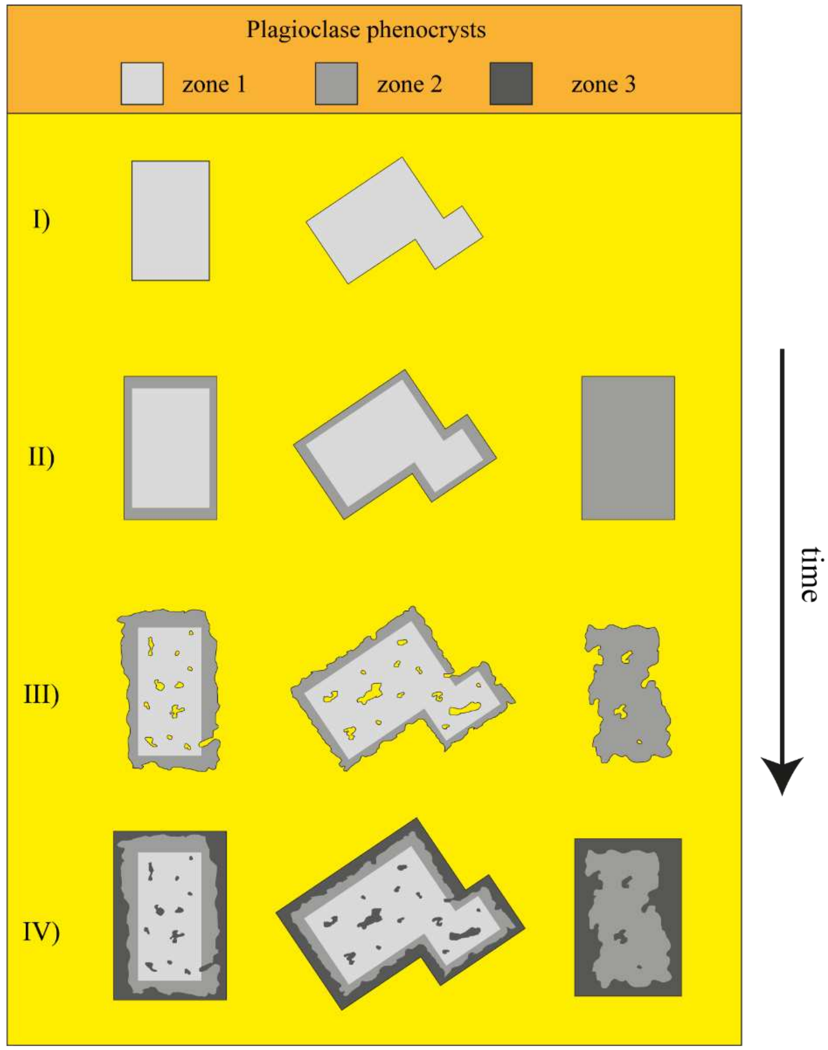

Figure 13. Evolution of plagioclase phenocrysts zoning over time: first event (I) is nucleation and growth of plagioclase phenocryst cores (Zone 1 composition); after that (II), growth of plagioclase phenocryst rims and nucleation and growth of new plagioclase phenocrysts occurred (Zone 2 composition). These two first crystallization events occurred during the crystal mush formation. After the crystal mush building, another process generating plagioclase-melt disequilibrium and resorption (we suggest volatile additions or heating) occurred (III), and finally (IV), a last growth event occurred. We infer that the last growth event occurred before or during the eruption triggering.

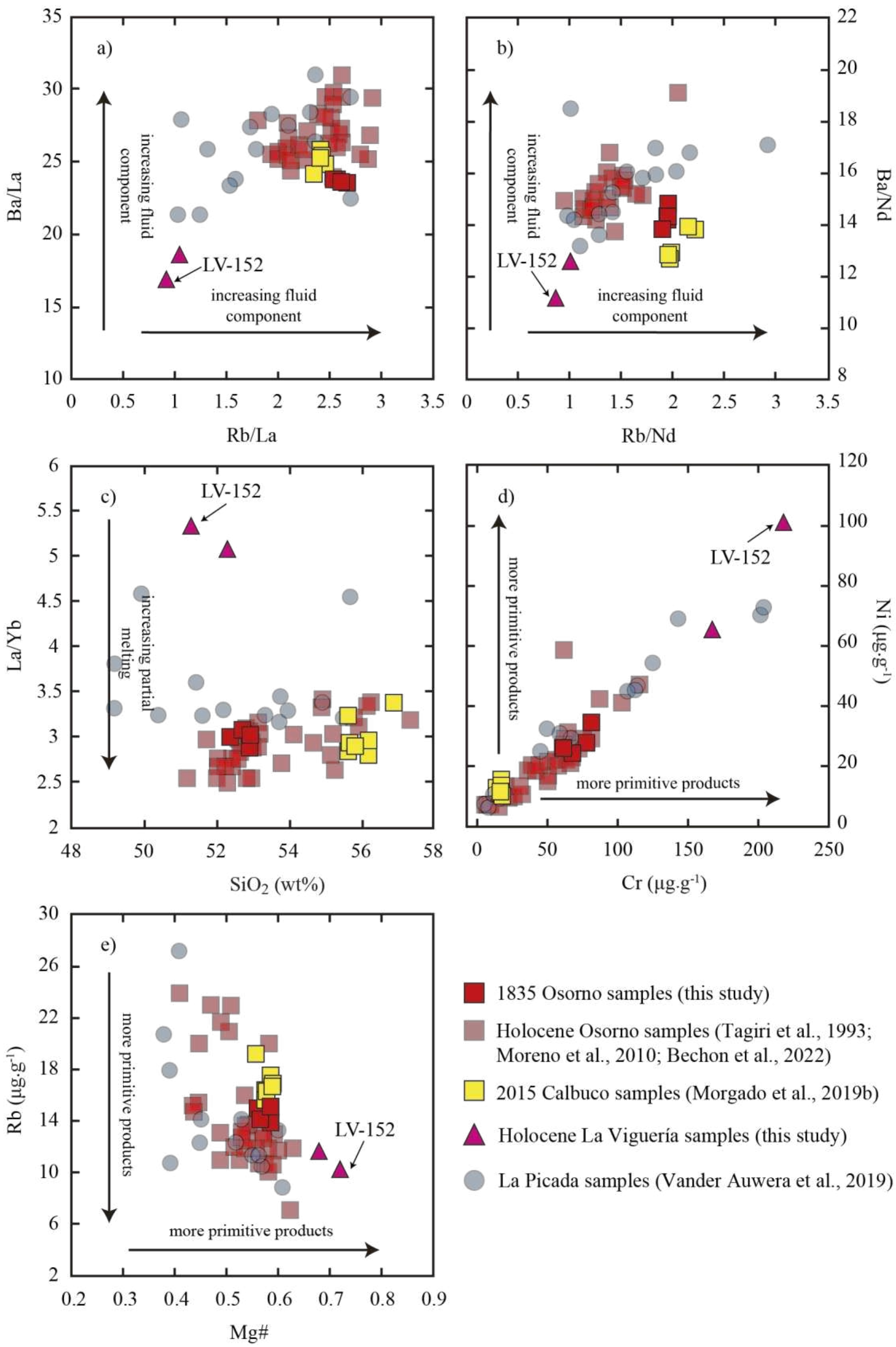

Figure 14. Plots of fluid mobile/immobile elements of Holocene volcanic samples of the region: (a) Ba/La versus Rb/La and (b) plot of Ba/Nd versus Rb/Nd. (c) plot of La/Yb versus

SiO_2. (d) plot of Ni ($\mu g \cdot g^{-1}$) versus Cr ($\mu g \cdot g^{-1}$). (e) plot of Rb ($\mu g \cdot g^{-1}$) versus Mg#. In a) and b) the arrows represent the direction in which the fluid component in the source is increasing. In c) the arrow represents the direction in which partial melting degree of the source is increasing. The arrows in d) and e) represent the direction in which the products are more primitive. We calculated Mg# assuming $Fe^{2+}/Fe^{3+} \approx 3$ (the same ratio we reported in this article via titration) in those samples from studies in which only $Fe_2O_{3(t)}$ is reported (Moreno et al., 2010; Bechon et al., 2022).

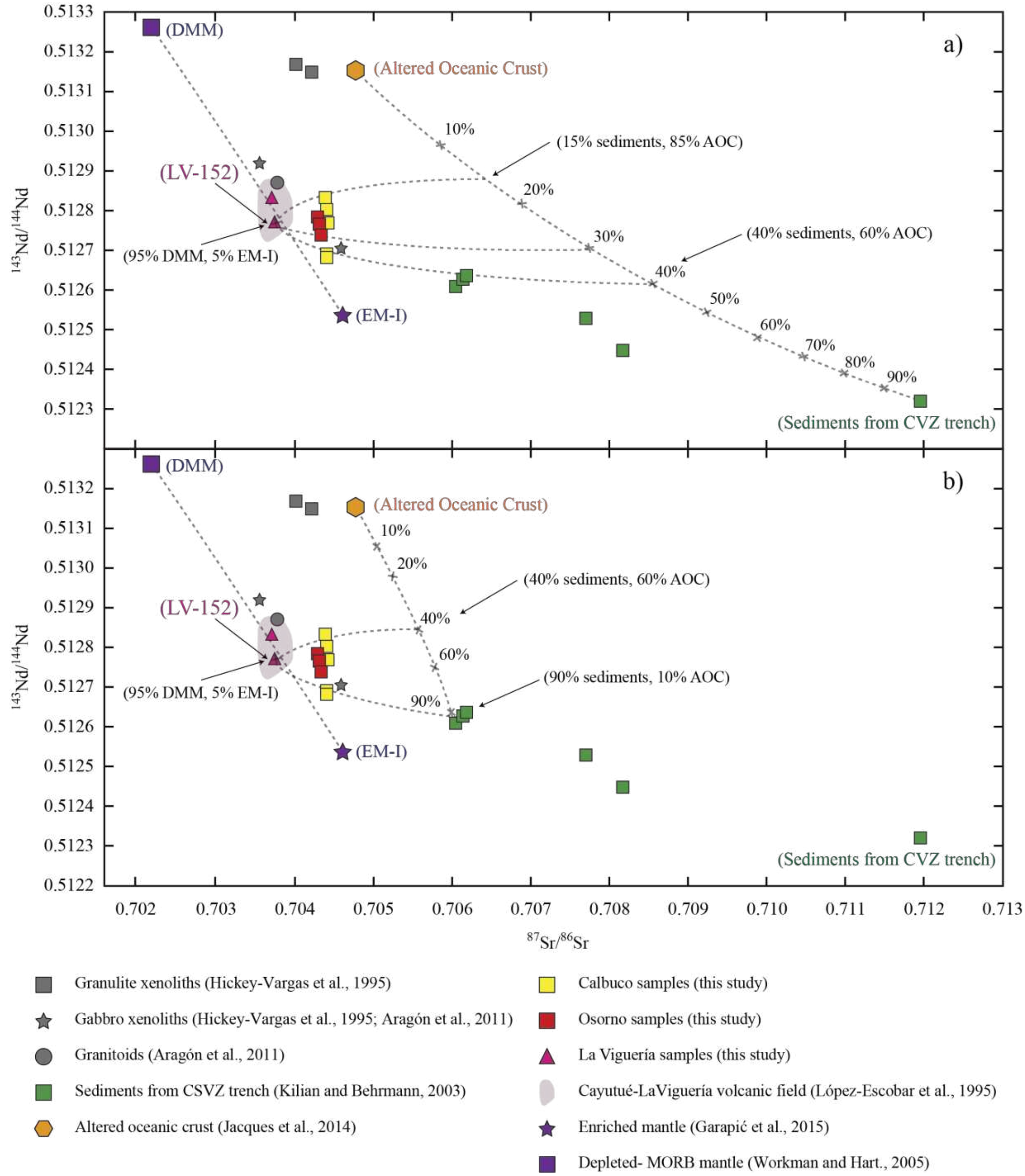

Figure 15. $^{143}Nd/^{144}Nd$ vs. $^{87}Sr/^{86}Sr$ of whole-rock compositions of the samples from the regional crustal rocks (granulite, gabbro, and granitoids; Hickey-Vargas et al., 1995; Aragón et al., 2011), Calbuco and Osorno stratovolcanoes, La Viguería small eruptive centre, and samples representing mantle compositions (DMM and EM-I; Workman and Hart, 2005; Garapić et al., 2015) and mixing lines showing possible fluid composition supplies considering the ranges of $^{87}Sr/^{86}Sr$ ratio and $^{143}Nd/^{144}Nd$ for trench sediments in Kilian and Behrmann (2003). The sediment compositional end-members are modelled in a) and b),

respectively. The mixing lines are built according to the isotopic values presented in Table 3.

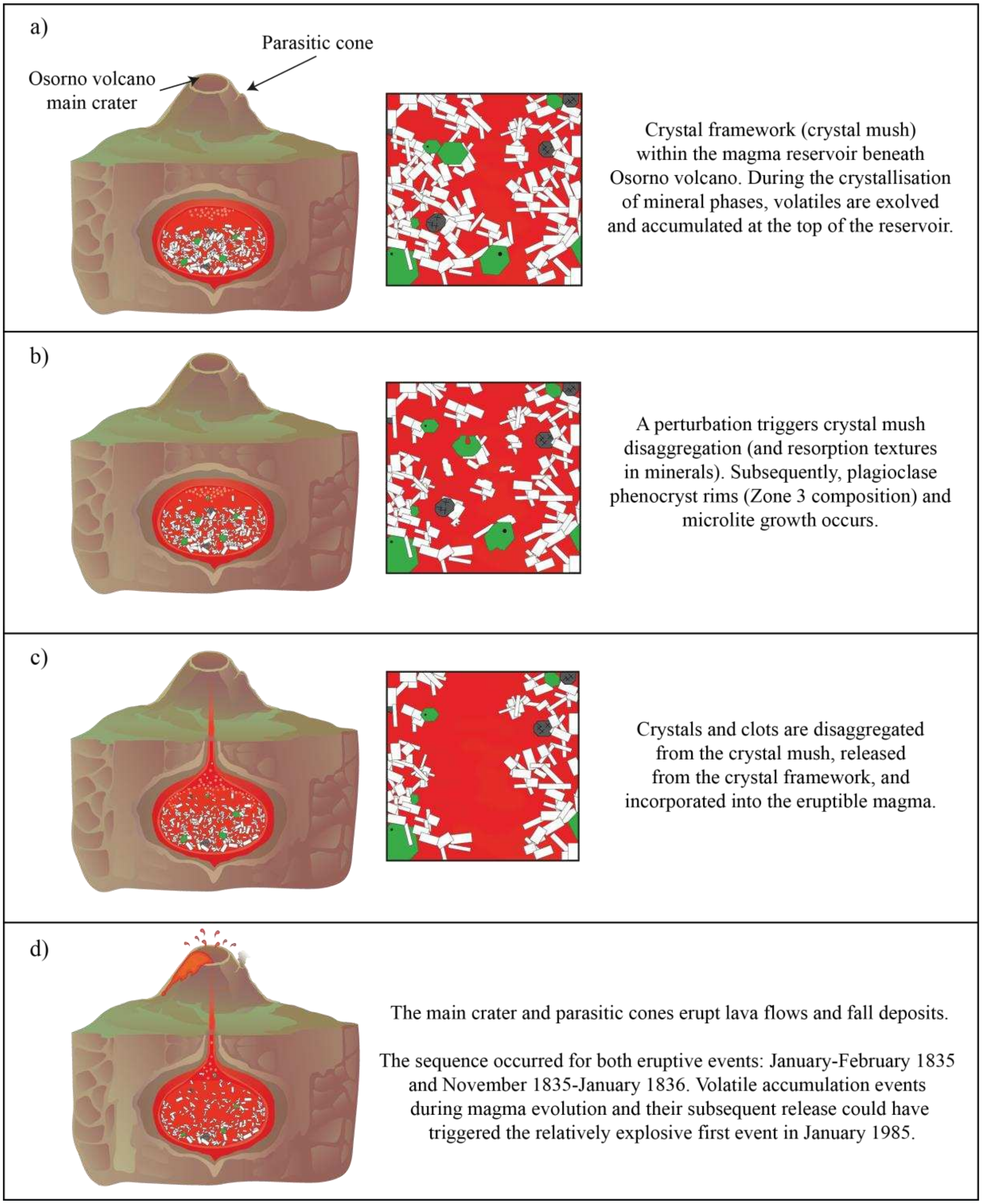

Figure 16. Schematic representation of the evolution of the shallow reservoir beneath Osorno volcano before the 1835 eruption. Figure (a) shows the initial crystal mush, which is perturbed (by heating and/or volatile addition), as represented in Figure (b). Figure (c) shows how crystals are disaggregated from the crystal mush and incorporated to the eruptible magma. Figure (d) shows when the eruption is triggered, it occurs in the main crater as well as the parasitic cones (image not to scale). The main crater and parasitic cones erupt lava

flows and fall deposits. The sequence occurred for both eruptive events: January-February 1835 and November 1835-January 1836. Volatile accumulation events during magma evolution and their subsequent release could have triggered the relatively explosive first event in January 1985.